View metadata, citation and similar papers at core.ac.uk
brought to you by CORE
provided by DepositOnce

ChemPubSoc Europe
DOI: 10.1002/cctc.201901705
Full Papers

Stannites – A New Promising Class of Durable Electrocatalysts for Efficient Water Oxidation

J. Niklas Hausmann,[a] Eva M. Heppke,[b] Rodrigo Beltrán-Suito,[a] Johannes Schmidt,[c] Martin Mühlbauer,[d] Martin Lerch,[b] Prashanth W. Menezes,*[a] and Matthias Driess*[a]

The oxygen evolution reaction (OER) through water oxidation is a key process for multiple energy storage technologies required for a sustainable energy economy such as the formation of the fuel hydrogen from water and electricity, or metal-air batteries. Herein, we investigate the suitability of Cu_2FeSnS_4 for the OER and demonstrate its superiority over iron sulfide, iron (oxy) hydroxides and benchmark noble-metal catalysts in alkaline media. Electrodeposited Cu_2FeSnS_4 yields the current densities of 10 and 1000 mA/cm^2 at overpotentials of merely 228 and 330 mV, respectively. State-of-the-art analytical methods are applied before and after electrocatalysis to uncover the fate of the Cu_2FeSnS_4 precatalyst under OER conditions and to deduce structure-activity relationships. Cu_2FeSnS_4 is the first compound reported for OER among the broad class of stannite structure type materials containing multiple members with highly active earth-abundant transition-metals for OER.

Introduction

Among the driving forces of global warming, the release of CO_2 into the atmosphere by burning fossils is one of the predominant factors.[1] An energy economy based on regenerative sources such as wind and sun is potentially carbon neutral.[2] A key requirement for the implementation of a sustainable energy economy is an efficient large scale energy storage technology such as the formation of fuels out of abundant and recyclable resources powered by electrical energy.[3,4] In this regard, electrocatalytic water splitting can be utilized to yield the carbon-neutral fuel hydrogen from electricity and water. Electrocatalytic water splitting is composed of two half-reactions: the hydrogen and oxygen evolution reaction (OER). The highest loss of efficiency in this process results from the overpotential (η) of the OER, which involves four sequential proton-coupled electron transfer steps.[5]

To overcome this disadvantage, a vast amount of suitable OER catalyst have been investigated.[6,7] Among these highly promising materials are transition-metal (TM) oxides, phosphates, chalcogenides, pnictides and carbides.[8,9] The strongly oxidizing conditions required to achieve the oxidation of water is in most cases accompanied by a more or less severe transformation of the materials to (oxy)hydroxides species.[10] Therefore, many of the oxides and most of the non-oxidic materials are merely precatalysts for the OER.[11] Even though the anion is often exchanged or depleted from the electrocatalytic active structure, it plays a significant role in tuning the properties of the active catalyst either by creating high surface areas and defects through leaching or by providing a conductive core.[10–15]

Bi- and multi-nuclear-TM (pre)catalysts have proven to be superior to mononuclear ones, as the variation of the metal composition enables the tuning of the intrinsic properties affecting the OER.[16,17] In this regard, it has been shown that an multinuclear assembling of metals helps to vary adsorption energies[2,18] and can afford higher stabilities,[19–21] conductivities[22–24] and surface areas[25,26] of OER catalysts.

An intensively investigated example is the inclusion of Fe into other TM systems such as Ni and Co.[27–36] In these materials, the included Fe cations drastically increase the OER activity, where Fe is proposed to act as the catalytically most active site.[27,30–33,37–38] However, poor catalytic activities are observed for heterometal-free FeO_xH_y,[37,39,40] due to its low electric conductivity.[29,37,41] Similarly, homometallic iron sulfides usually show low catalytic activities for the OER.[8,42] An exception represent pyrrhotite Fe_7S_8 nanosheets bearing mixed Fe valence states and metallic conductivity.[42] On the contrary to homometallic iron sulfides, heterobi- and heteromulti-metallic iron sulfides and especially selenides belong to the most active OER catalysts reported yet.[5,43,44]

[a] J. N. Hausmann, R. Beltrán-Suito, Dr. P. W. Menezes, Prof. Dr. M. Driess
Department of Chemistry: Metalorganics and Inorganic Materials
Technische Universität Berlin
Straße des 17 Juni 135, Sekr. C2, 10623 Berlin (Germany)
E-mail: prashanth.menezes@mailbox.tu-berlin.de
matthias.driess@tu-berlin.de
[b] E. M. Heppke, Prof. Dr. M. Lerch
Department of Chemistry: Solid State Chemistry
Technische Universität Berlin
Strasse des 17. Juni 135, Sekr. C2, 10623 Berlin (Germany)
[c] Dr. J. Schmidt
Department of Chemistry: Functional Materials
Technische Universität Berlin
Hardenbergstraße 40, 10623 Berlin (Germany)
[d] Dr. M. Mühlbauer
Heinz Maier-Leibnitz Zentrum (MLZ)
Technische Universität München
Lichtenbergstraße 1, 85748 Garching (Germany)

Supporting information for this article is available on the WWW under https://doi.org/10.1002/cctc.201901705

This manuscript is part of the Special Issue "Electrocatalysis: From Batteries to Clean Energy Conversion", which is part of the wider project "Building A New Energy Economy with Catalysis".

© 2019 The Authors. Published by Wiley-VCH Verlag GmbH & Co. KGaA. This is an open access article under the terms of the Creative Commons Attribution License, which permits use, distribution and reproduction in any medium, provided the original work is properly cited.

© 2019 The Authors. Published by Wiley-VCH Verlag GmbH & Co. KGaA

Quaternary sulfides or selenides of the formula $A_2^{+I}B^{+II}C^{+IV}X_4^{-II}$ usually contain three different metals. A great variety of (semi)metals can be implemented for example A = Li, Na, Ag, Cu; B = Mn, Fe, Co, Ni, Zn, Cd; and C = Si, Ge, Sn.[45–52] Many members of this class of materials crystallize in the stannite structure type named after the mineral stannite with the formula Cu_2FeSnS_4. The stannite-type structure (space group $I\bar{4}2m$, see unit cell in Figure 1) can be described as a cubic closed packed array of anions with half of the tetrahedral voids filled with cations. Its basis is the cubic diamond structure and all atoms are coordinated tetrahedrally by their closest neighbors. Stannites have been intensively investigated, due to their application as thin film solar cells.[53–56] In this regard, comprehensive efforts have been undertaken to fabricate thin films thereof.[57–59] This expertise could be used to realize stannite-based electrodes and to probe the material for its OER suitability. To the best of our knowledge, stannite-type materials have not been tested yet as OER precatalysts.

Herein, we report the superior electrocatalytic properties of Cu_2FeSnS_4 on fluorine doped tin oxide (FTO) and nickel foam (NF) compared to iron sulfide, iron (oxy)hydroxide and the benchmark noble-metal precatalysts IrO_2 and RuO_2. We found that Cu_2FeSnS_4 acts as a precursor for the catalytically active phase, where tin is depleted completely from the active structure and sulfur leaches as well in the form of elemental S_8. The severe structural changes lead to an X-ray amorphous high surface area structure containing nanocrystalline FeOOH embedded into an amorphous copper-containing matrix. This nanocomposite shows a significantly reduced charge transfer resistance (R_{ct}) compared to the pure iron component, most likely due to an improved electron transport to the FeOOH nanocrystallites. The presented results demonstrate the great potential of stannites for efficient OER. Bearing in mind that stannites containing the most active earth-abundant TM are synthetically accessible;[50] this report may triggers further interest to explore the OER properties of this class of quaternary materials.

Results and Discussion

Structural Characterization of Cu_2FeSnS_4

Cu_2FeSnS_4 was synthesized by mechanochemical milling starting from the respective binary sulfides and followed by annealing in a tube furnace.[60] All reflections of the neutron diffraction pattern depicted in Figure 1 (top) could be unambiguously assigned to the stannite structure with space group $I\bar{4}2m$ and the unit cell parameters a = 5.451 Å and c = 10.746 Å (see Tabs. S1 and S2 in the supporting information for refinement data). Further, a powder X-ray diagram (pXRD) is shown in Figure S1 confirming the neutron diffraction data. The cations

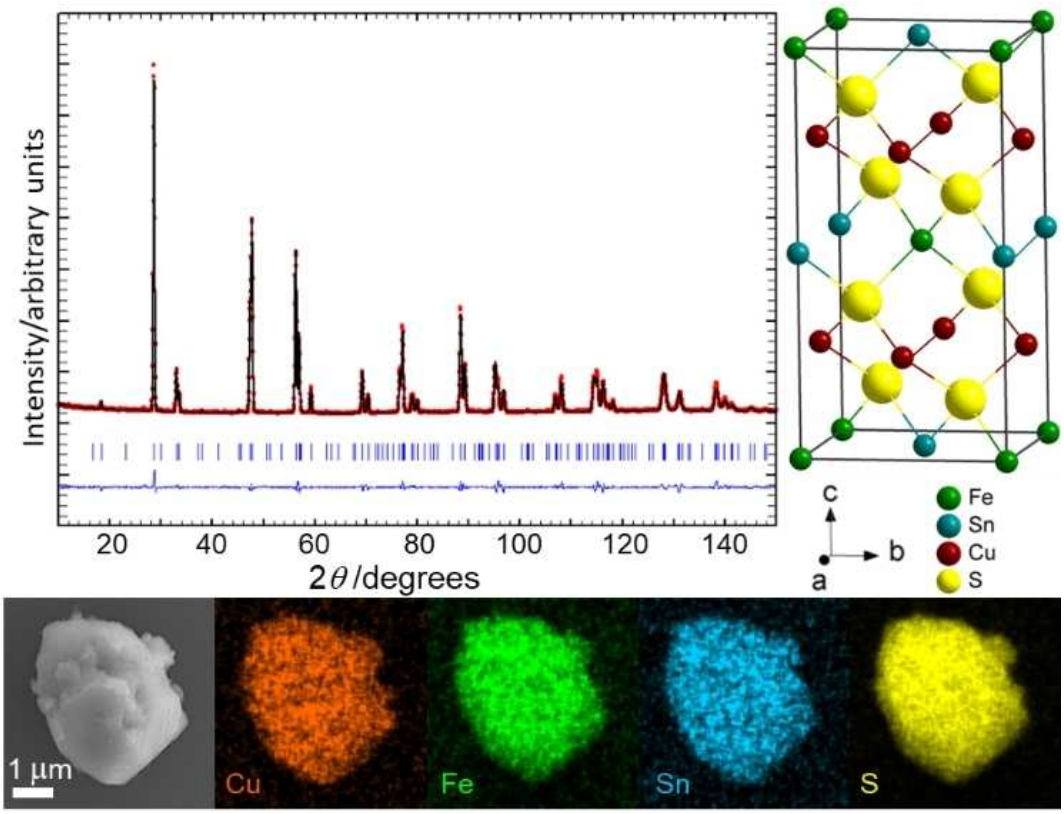

Figure 1. Top: Neutron diffraction pattern (red points) of stannite, Cu_2FeSnS_4, with Rietveld refinement (black line), difference (blue line), Bragg reflections (blue stripes) and unit cell on the right. Bottom: SEM/EDX mapping of a Cu_2FeSnS_4 particle.

© 2019 The Authors. Published by Wiley-VCH Verlag GmbH & Co. KGaA

are arranged in $Cu^{(I)}$–$Cu^{(I)}$ layers alternating with $Fe^{2+(II)}$–$Sn^{4+(IV)}$ layers in the tetrahedral voids of the cubic closed packed $S^{2(-II)}$ anionic partial structure (see Figure 1, top left). The scanning electron microscopy (SEM) images displayed in Figure S3 exhibit the formation of particles without a clearly defined morphology and a size ranging from 0.1 to 4 μm. Further, energy dispersive X-ray (EDX) mapping using SEM was conducted to determine the elemental distribution in Cu_2FeSnS_4. The images shown in Figure 1 (bottom) confirm a homogeneous distribution of the elements Cu, Fe, Sn and S, and the EDX spectrum excludes the presence of other elements (see Figure S3). Additionally, inductively coupled plasma atomic emission spectroscopy (ICP-AES) yielded an elemental ratio of 2.1:1.0:1.0:4.2 of Cu:Fe:Sn:S, which is in accordance to the formula composition (see Tab. S3). The selected area diffraction pattern (SAED) obtained by transmission electron microscopy (TEM) shows bright diffraction spots confirming the highly crystalline nature of the material (see Figure S4 (a)). The crystallographic planes (112), (004), (204), (301) and (224) could be assigned in agreement with the neutron diffraction data. High-resolution TEM images display a lattice spacing of 0.521 nm and 0.314 nm revealing the crystallographic planes (002) and (112) (see Figure S4 (e) and (f)).

The surface bonding and oxidation states of Cu_2FeSnS_4 were unveiled by X-ray photoelectron spectroscopy (XPS). The Cu 2p, Fe 2p, Sn 3d and S 2p spectra (see Figure S5) exhibit the expected oxidation states of Cu^{I}, Fe^{II}, Sn^{IV} and S^{-II} with minor amounts of Cu^{II} and a significant amount of S^{IV} caused by surface oxidation. These data are consistent with those reported for Cu_2FeSnS_4 in the literature.[54]

Electrocatalytic Characterization and OER Performance

The electrocatalytic activity of the Cu_2FeSnS_4 towards the OER was investigated in 1 M aqueous KOH using linear sweep voltammetry (LSV). The Cu_2FeSnS_4 was first electrophoretically deposited on a 2×1 cm^2 FTO glass plate substrate with a mass loading of 1 mg on an area of 1 cm^2 (see Figure S6 for pXRD from Cu_2FeSnS_4/FTO). The LSVs of Cu_2FeSnS_4 and the reference iron materials attained at a scan rate of 5 mV/s are shown in Figure 1 (a). The overpotentials of 365 and 550 mV are needed for Cu_2FeSnS_4 to reach current densities of 10 and 100 mA/cm^2, respectively. This is significantly less than in case of FeS/FTO, Fe$(OH)_3$/FTO and FeOOH/FTO with the same mass loading as well as bare FTO, even though the weight percent of iron in Cu_2FeSnS_4 (13%) is much lower compared to the sulfides and oxides.

Motivated by this promising result, we loaded 2 mg of the same materials on NF. NF has recently become an attractive choice as an electrode material, due to its low cost along with a high conductivity, large electro-active surface area, impeccable mechanical stability and good corrosion resistance.[61,62] Further, its 3D porosity enhances the catalyst-substrate contact for efficient electron transport and lowers electrolyte mass transport limitations. SEM images and an EDX mapping of Cu_2FeSnS_4/NF are displayed in Figures S7 and S8. LSV scans with NF based electrodes loaded with Fe containing materials are shown in Figure 2 (b). They were obtained by cycling in a potential range of 1.15 to 1.58 V with a scan rate of 5 mV/s until three similar consecutive scans were obtained. Bare NF treated under the same applied electrophoretic deposition (EPD) potentials in similar conditions exhibited a deplorable OER

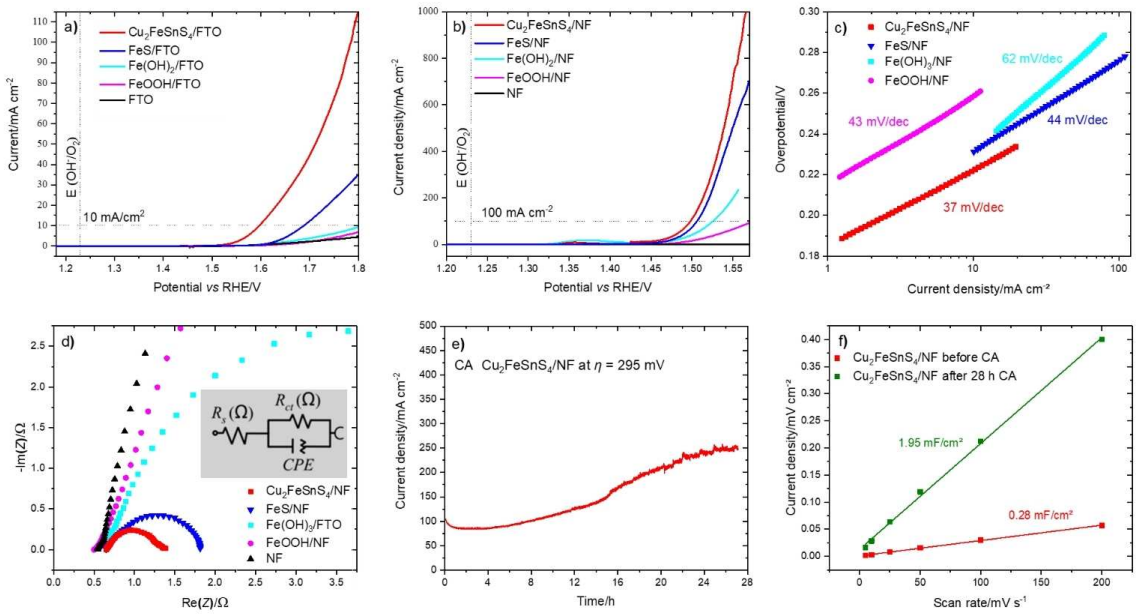

Figure 2. (a) LSV (5 mV/s) of Cu_2FeSnS_4 and various Fe containing materials loaded on FTO (1 mg/cm^2), (b) LSV (5 mV/s) of various materials loaded on NF (2 mg/cm^2), (c) Tafel slopes obtained from LSV (1 mV/s), (d) EIS responses ($R_{ct}(Cu_2FeSnS_4) = 0.64\ \Omega$ and $R_{ct}(FeS) = 1.18\ \Omega$), (e) long term CA measurement, (f) linear fits (derived by Figure S10) to obtain C_{dl} of the as prepared electrode and after CA measurement (e).

© 2019 The Authors. Published by Wiley-VCH Verlag GmbH & Co. KGaA

activity. The overpotentials of Cu_2FeSnS_4/NF to reach the current densities of 10, 100 and 1000 mA/cm^2 were 228, 267 and 330 mV, respectively. The activity trend for the iron-based materials were the same as on FTO. Additionally, the benchmark noble metal-based catalysts MO_x (M=Ru, Ir) were deposited on NF and investigated similarly (see Figure S9 (a)). Most notable, Cu_2FeSnS_4/NF shows a significantly higher activity than these reference materials. Furthermore, we synthesized the referring homo- and heterobi-metallic phases SnS, CuS, Cu_2SnS_3 and $CuFeS_2$ following exactly the same synthetic procedure as done for Cu_2FeSnS_4. The referring pXRDs are shown in Figure S23. These four materials were investigated similarly concerning their OER performance (see Figure S9 (b)). This investigation reveals that the activity increases in the order SnS < CuS < Cu_2SnS_3 < $CuFeS_2$ < FeS < Cu_2FeSnS_4. Two conclusion can be deduced from this activity trend: (i) Fe is crucial to obtain a high electrocatalytic activity and most likely the active site and (ii) the trimetallic stannite phase is indeed required to achieve an exceptional electrocatalytic performance.

To gain insight into the electrocatalytic kinetics, Tafel plots (see Figure 2 (c)) were obtained from LSVs with a scan rate of 1 mV/s. Cu_2FeSnS_4/NF showed the lowest Tafel slope of the investigated electrodes with 37 mV/dec indicating a higher transfer coefficient and superior OER kinetics.[6] This value is in the range (~30–45 mV/dec) of FeOOH and other bi- and multinuclear-TM, iron-containing oxyhydroxides and identical with the Tafel slope obtained for Cu_2FeSnS_4/FTO (see Figure S10).[23] This result suggests that in both cases iron is the catalytically active site. The linear Tafel behavior could be observed until a current density of 11 mA/cm^2 for Cu_2FeSnS_4/NF in contrast to <1 mA/cm^2 for Cu_2FeSnS_4/FTO, indicating that other effects such as surface coverage or electron/proton transport are influencing the catalytic behavior on FTO negatively at much lower current densities already.[63–65] Hence, the utilization of NF as an electrode substrate proved to be suitable to overcome these disadvantages to a certain extent.

Additionally, electrochemical impedance spectroscopy (EIS) was performed to evaluate the electrode transfer kinetics under OER conditions.[66] As shown in Figure 2 (d), Cu_2FeSnS_4 possesses a significantly smaller charge transfer resistance (R_{ct}) than the other aforementioned iron-based catalysts on NF. On FTO the R_{ct} of Cu_2FeSnS_4 is seven times smaller than the one of FeS and more than 28 times smaller than the lowest one of the investigated FeO_xH_y catalysts (see Figure S10). This reveals superior electron transfer and catalytic kinetics, in agreement with the Tafel data.

Chronoamperometry (CA) at an overpotential of 295 mV was performed over a period of 27 h to investigate the stability under comparably high current densities (see Figure 2 (e)). Initially, a current density of 100 mA/cm^2 was obtained, but a constant increase could be observed in the first 24 h until the current response stabilized at 250 mA/cm^2. This proves the excellent stability and activity of the investigated system.

We determined the electrochemical double-layer capacitance (C_{dl}), which is proportional to the electrochemically active surface area (ECSA), by performing cyclic voltammetry with different scan rates in a potential range, where no apparent Faradaic process occurred (see Figure 2 (f)). Before electrocatalytic testing, a value of 0.28 mF/cm^2 for Cu_2FeSnS_4/NF was obtained. After the CA measurement, the C_{dl} increased to 1.95 mF/cm^2 (see Figure 2 (f)) revealing a transformation of the material during OER conditions to a phase with multiple times higher ECSA.

To rule out that other oxidation reactions such as the oxidation of $S^{2(-II)}$ are responsible for the high currents observed, we performed two Faradaic efficiency tests at different current densities. In a closed electrochemical cell Cu_2FeSnS_4/NF, after performing a CA measurement at $\eta =$ 295 mV for 1 h, was used as an anode and CP measurements at 10 mA/cm^2 and 100 mA/cm^2 for 8 min and 2 min were performed. The resulting quantity of O_2 was compared to the current and the Faradaic efficiencies of 94% and 96% were obtained for the experiment at 10 and 100 mA/cm^2, respectively.

Post Catalytic Characterization

Even though Cu_2FeSnS_4 does not show any changes by pXRD or ICP after several hours of 1 M KOH exposure (see Table S3), the electrocatalytic tests indicate a transformation of the material during OER conditions induced by the strongly oxidizing potential. Thus, to gain in-depth insight into the structural transformation, and, therefore, the origin of the prominent electrocatalytic activity, we characterized Cu_2FeSnS_4 after CA measurements with pXRD, SEM, EDX, TEM and XPS.

A pXRD measurement taken directly from the FTO substrate after electrocatalytic testing (Cu_2FeSnS_4/FTO/OER) reveals the absence of every reflex of the original Cu_2FeSnS_4 structure (see Figure S12). Instead, reflexes with a significant weaker intensity are present, which were unambiguously assigned to elemental sulfur. SEM measurements (see Figures 3 (a) and S13) of the same electrode show the absence of the irregular shaped particles with a size close to 1 μm as present in the as-prepared material (see Figure S2) and the deposited one (see Figure S7). Instead, a nanoscale rough morphology with a high surface area is present. EDX mapping (see Figure S13) displays particles containing only sulfur; one of these is indicated in Figure 3 (a). The EDX spectrum (see Figure S14) unveils that only Cu, Fe, K and O are present after the electrocatalytic testing in an area without a sulfur particle. For Cu_2FeSnS_4/NF/OER, the SEM and EDX (see Figures S16–S18) results are similar even though the morphology of the nanoscale rough surface differs.

TEM investigations were performed by scratching off used catalyst from a Cu_2FeSnS_4/FTO/OER electrode. The images taken at various magnifications (see Figures 3 (c) and S15) show nanoparticles with a rough morphology and high surface area. The selected area electron diffraction (SAED) presented in Figure 3 (b) exhibits two broad rings indicating nanocrystallinity. The SAED intensities fit perfectly well to the one of the iron oxyhydroxide, 2-line ferrihydrite, and lattice distances determined from diffraction rings are in good agreement with the crystallographic (110) and (106) planes of 2-line ferrihydrite.[67,68] In the HR-TEM image shown in Figure 3 (d), ordered and

© 2019 The Authors. Published by Wiley-VCH Verlag GmbH & Co. KGaA

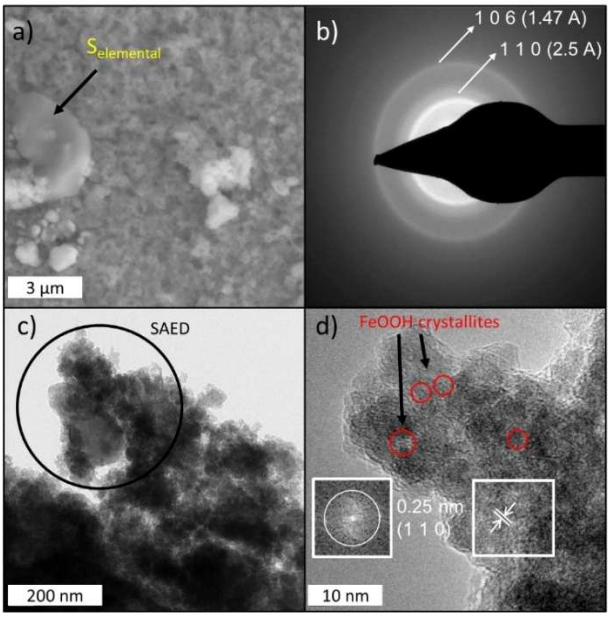

Figure 3. Electron microscopy of Cu_2FeSnS_4 after OER: (a) SEM image, the arrow indicates a particle of elemental sulfur, (b) SAED with crystallographic planes of FeOOH, (c) TEM image, the black circle indicates the area of the SAED, (d) HR-TEM image with the Fourier transformation of the selected area revealing fringes of the crystallographic plane (110) of FeOOH, the red circles indicate regions of uninterrupted ordered lattice fringes.

uninterrupted lattice fringes can be seen in an area of up to at most 2 nm diameter. The Fourier transform of such an area reveals a lattice spacing of 0.25 nm, consistent with the (110) crystallographic plane of 2-line ferrihydrite. The fact that the uninterrupted, ordered crystalline domains are so small leads to a large amount of disordered iron surface sites that can act as catalytic centers. No crystalline phase containing copper could be found, and therefore, we assume that copper is present in form of an amorphous matrix in between the FeOOH nanocrystallites.

Figure 4 shows the Cu 2p, Fe 2p and O 1s XPS spectra of a sample of the Cu_2FeSnS_4/FTO/OER electrode material. The Cu $2p_{3/2}$ and Cu $2p_{1/2}$ spectrum exhibits sharp peaks at the binding energy of 931.9 and 951.7 eV, indicating the presence of a Cu^{I} species.[69] Additionally, satellite peaks typical for Cu^{II} are located at the binding energies of 939.9, 942.6 and 961.2 eV.[14,69] The low intensity of these satellites is in agreement with the deconvolution of the Cu $2p_{3/2}$ and Cu $2p_{1/2}$ peaks, revealing that most of the Cu is in the Cu^{I} state with a minor contribution of Cu^{II}. The presence of mainly Cu^{I} species strongly supports the hypothesis that iron is the actual active site and that the role of copper is likely another one such as facilitating electron transport. This is further indicated by the low R_{ct} of Cu_2FeSnS_4/FTO compared to the other copper-free iron compounds investigated by EIS (see Figure S10). The Fe core-level spectrum (see Figure 4 (b)) exhibits two major, rather broad peaks located at 710.1 eV for Fe $2p_{3/2}$ and 723.6 eV for Fe $2p_{1/2}$. These binding energies are in-between those expected for Fe^{II} and Fe^{III}.[70,71] The Fe $2p_{3/2}$ peak overlaps with the ones of Sn 3p and Cu LM5/6 located at slightly higher binding energies. However, no additional peaks interfere with the Fe $2p_{1/2}$ region allowing a deconvolution of Fe 2p signals originating from Fe^{II} and Fe^{III}. Such an analysis reveals the coexistence of these two oxidation states in approximately equal amounts. The presence of Fe^{III} is further supported by the satellite peak at 732.0 eV.[70,71] The increased oxidation state strengthens the hypothesis that iron is the catalytically active site, as indicated already by the Tafel slope of 37 mV/dec.[23] The O 1s core-level spectrum reveals a peak with two maxima and one shoulder, suggesting the presence of at least three chemically distinct oxygen environments. The deconvoluted XPS spectrum of pure FeOOH[71] exhibits three peaks at similar binding energies like those shown in Figure 4 (c). These peaks could be assigned to Fe–O–Fe, Fe–O–H and surface absorbed water.[71–73] This confirms the conclusion of the TEM results that FeOOH, 2-line ferrihydrite, nanocrystallites are formed during OER conditions. However, other metal oxide such as the SnO_2 from the FTO overlap with these peaks. This can be clearly seen if one

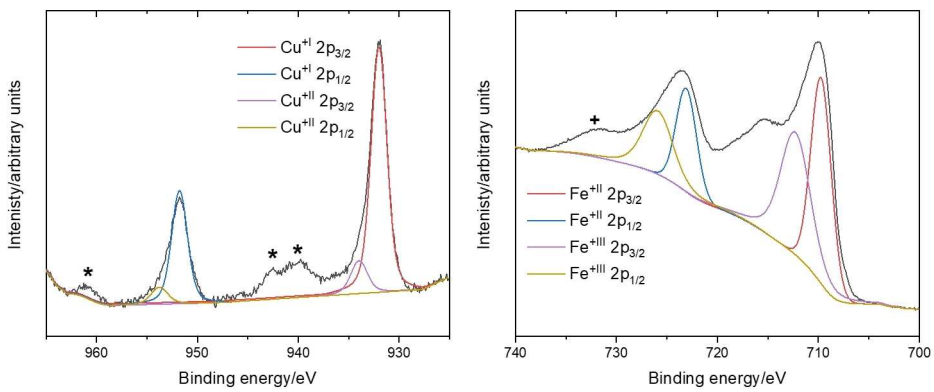

Figure 4. XPS analysis of Cu_2FeSnS_4/FTO/OER; (a) Cu 2p spectrum with Cu^{II} satellites marked with *; (b) Fe 2p spectrum with Fe^{III} satellites marked with +; (c) O 1s spectrum.

© 2019 The Authors. Published by Wiley-VCH Verlag GmbH & Co. KGaA

compares the O 1s core-level spectrum of Cu_2FeSnS_4/FTO/OER to the one of Cu_2FeSnS_4/NF/OER shown in Figure S19. The metal oxide peak is strongly reduced in the Cu_2FeSnS_4/NF/OER spectrum, as no SnO_2 is present. The Cu and Fe 2p spectra of Cu_2FeSnS_4/NF/OER are also displayed in Figure S19 and indicate the same oxidation states in slightly different ratios than those found for Cu_2FeSnS_4/FTO/OER.

Conclusions

Herein, the superior electrocatalytic properties of Cu_2FeSnS_4 on FTO and NF compared to single component iron sulfide, iron (oxy)hydroxide and the benchmark noble-metal-based catalyst MO_x (M=Ru, Ir) with the same mass loading are presented. We reveal that Cu_2FeSnS_4 consisting only out of earth-abundant elements acts as a precursor for the catalytically active phase, which is nanocrystalline FeOOH embedded into an amorphous copper-containing matrix. This phase is formed by the complete depletion of tin and sulfur and severe reorganization of the precursor structure. We could identify three major reasons for the superior electrocatalytic activity: First, a significantly increased surface area caused by the *in-situ* formed nanoscale rough morphology, second, an improved R_{ct} most likely caused by a facilitated electron transport through the presence of mixed-valence $Cu^{I/II}$, and third, a large amount of disordered Fe surface sites of the X-ray amorphous nanocrystalline (<2 nm) FeOOH. Cu_2FeSnS_4 is the first stannite material reported for OER. As stannites are known containing the most OER active earth-abundant elements, this report opens a new avenue to novel, highly efficient and robust OER catalysts.

Experimental Section

Materials and synthesis

1 M aqueous KOH and other reagents used in the synthetic procedures were obtained from Sigma Aldrich. The commercial RuO_2 (99%) and IrO_2 (99%) were purchased from Alfa Aesar. NF and FTO (resistivity 8–12 Ω/sq) were purchased from Recemat BV and Sigma Aldrich, respectively.

Cu_2FeSnS_4. Cu_2FeSnS_4 was synthesized by mechanochemical milling in a high energy planetary Mono Mill PULVERISETTE 6 (Fritsch, Idar-Oberstein, Germany) starting from the binary sulfides and followed by an annealing procedure in a tube furnace.[61] Stoichiometric amounts of CuS, FeS_2 (Sigma Aldrich, 99.8%) and SnS were filled in a 45 ml zirconia grinding beaker with six zirconia grinding balls (diameter 15 mm) and milled at a rotational speed of 350 rpm for five hours. In order to obtain a highly crystalline product, the ground material was annealed in a subsequent step at 1023 K for two hours under flowing reaction gas (H_2S). The Cu_2FeSnS_4-sample was quenched from 1023 K to room temperature to avoid phase transformation from the high-temperature stannite-type polymorph (space group $I\bar{4}2m$) to low-temperature phase in space group $P\bar{4}$. CuS was prepared by precipitation from a 0.1 M $Cu(NO_3)_2$ solution with H_2S (Air Liquide, 99.5%) followed by annealing at 503 K for two hours in H_2S-atmosphere. For SnS a solid-state reaction of tin (Merck, 99.9%) and sulfur (Fluka, 99.99%) in an evacuated and sealed silica glass ampoule was applied.

FeS, $Fe(OH)_3$ & FeOOH. Amorphous $Fe(OH)_3$ was synthesized by precipitation of an iron(III) nitrate following a reported protocol and FeOOH by precipitation of iron(II) sulfate followed by oxidation with H_2O_2.[74,75] Hexagonal crystalline FeS was synthesized by a solid-state reaction following a reported protocol.[76] The corresponding pXRD data to the three materials can be found in the supporting information (see Figures S19 and S20).

Characterization

Powder X-ray and neutron diffraction. A Panalytical X'Pert PRO diffractometer (Bragg-Brentano geometry, Cu-K_α radiation) was used for powder XRD measurements. Neutron powder diffraction data were collected at the Forschungs-Neutronenquelle Heinz-Maier-Leibnitz Zentrum (MLZ, Garching) using the high-resolution powder diffractometer SPODI (Ge (551) $\lambda = 1.54816$ Å). For neutron experiments the sample was encapsulated in a vanadium container with 0.15 mm wall thickness and 9 mm inner diameter (Ar atmosphere). Structural refinements were performed by the Rietveld method[77] using the program FULLPROF[78] Suite Version 2015 by applying a Thompson-Cox-Hastings pseudo-Voigt function for the neutron data, respectively.

Inductively coupled plasma atomic emission spectroscopy. ICP-AES was conducted on a Thermo Jarrell Ash Trace Scan analyser. The materials were digested in aqua regia HCl: HNO_3 4:1 v/v (nitric acid, SUPRA-Qualität ROTIPURAN® Supra 69% and hydrochloric acid, SUPRA-Qualität ROTIPURAN® Supra 30%). The digestion volume (2.5 ml) was diluted with milli-Q water up to 10 ml. Calibration curves were prepared for copper, iron, tin and sulfur with concentrations between 1 mg/l and 100 mg/l from standard solutions (1000 mg/l Single-Element ICP-Standard Solution ROTI STAR).

Scanning electron microscopy. SEM was performed on a Gemini-SEM500 NanoVP microscope (ZEISS) integrated with an EDX detector (Bruker Quantax XFlash® 6|60). The most abundant elements were selected from the EDX spectrum. Data handling and analysis were achieved with the software package EDAX. The SEM experiments were conducted at the Zentrum für Elektronenmikroskopie (ZELMI) of the TU Berlin.

Transmission electron microscopy. TEM was performed on an FEI Tecnai G2 20 S-TWIN transmission electron microscope (FEI Company, Eindhoven, Netherlands) equipped with a LaB_6 source at 200 kV acceleration voltage. For the investigation of the films after electrocatalysis, the films were scraped from the electrode substrate and transferred onto a carbon-coated copper grid. EDX analyses were achieved with an EDAX r-TEM SUTW detector (Si (Li) detector), and the images were recorded with a GATAN MS794 P CCD camera. The TEM experiments were conducted at the Zentrum für Elektronenmikroskopie (ZELMI) of the TU Berlin.

X-ray photoelectron spectroscopy. XPS measurements were carried out using a ThermoScientific K-Alpha+ X-ray photoelectron spectrometer. All samples were analysed using a microfocused, monochromated Al-K_α X-ray source (1486.68 eV; 400 μm spot size). The analyser had a pass energy of 200 eV (survey), and 50 eV (high-resolution spectra), respectively. Binding energies were calibrated to the C 1s peak at 284.8 eV. To prevent any localized charge build up during analysis the K-Alpha+ charge compensation system was employed at all measurements. The samples were mounted on conductive carbon tape or measured directly from the electrode substrates (FTO and NF). The resulting spectra were analysed using the Avantage software from ThermoScientific.

© 2019 The Authors. Published by Wiley-VCH Verlag GmbH & Co. KGaA

Electrochemical measurements

All measurements were performed at 25 °C regulated by a thermostat. A typical electrocatalytic run was carried out in a standard three-electrode (working, counter and reference) electrochemical cell in 50 ml 1 M aqueous KOH with a potentiostat (SP-200, BioLogic Science Instruments) controlled by the EC-Lab v10.20 software package. The electrodes (NF/FTO) with samples deposited served as the working electrodes, Pt wire (0.5 mm diameter × 230 mm length; A-002234, BioLogic) as a counter and Hg/HgO as the reference electrode (CH Instruments, Inc.).

Cyclic and linear sweep voltammetry. CV and LSV was performed without stirring and with an applied iR compensation of 90%. The uncompensated resistance (R_u) was acquired by impedance spectroscopy at 100 MHz. The potentials of the reference electrodes in this work were referenced to the reversible hydrogen electrode (RHE) through calibration, and in 1 M aqueous KOH the potential was calculated using the following equation [Eq. (1)]:

$$E(\mathrm{RHE}) = E(\mathrm{Hg/HgO}) + 0.098\,\mathrm{V} + (0.059 \times \mathrm{pH})\ \mathrm{V} \quad (1)$$

Chronoamperometry. The CA measurements were performed with intensive stirring and an applied iR compensation of 90% in 1 M aqueous KOH at selected constant potentials with respect to RHE.

Tafel analysis. The Tafel slope was calculated according to the Tafel equation $\eta = b\log j + a$, where η is the overpotential (V), j is the current density (mA/cm^2), and b is the Tafel slope (mV/dec).

Double-layer capacitance. C_{dl} was determined from the CV (cycled between 0.875 and 0.925 V vs. RHE) at a potential range, where no apparent faradaic process occurred. The anodic charging currents measured at 0.9 V vs. RHE were plotted as a function of the scan rate and from the slope the C_{dl} was attained.[79–81] The ECSA of the catalysts can be calculated using the equation ECSA $= C_{dl}/C_s$, where C_s can be defined as the specific capacitance of the material per unit area under identical electrolyte conditions.[82] Therefore, the ECSA is directly proportional to C_{dl}.

Electrochemical impedance spectroscopy. EIS was recorded at 1.57 V vs. RHE for FTO samples and at 1.49 V vs RHE for NF samples to obtain the Nyquist plots. The amplitude of the sinusoidal wave was examined in a frequency range of 100 kHz to 1 mHz. All impedance spectra were fitted using an equivalent RC circuit model. The charge-transfer resistance (R_{ct}) was then obtained from the diameter of the semicircle in the Nyquist plots.[79,82]

Electrophoretic deposition. The investigated materials were deposited electrophoretically by a well-established method on both, NF and FTO.[62,75,82–84] A potential difference of 10 V, using FTO as both counter and reference electrode or NF for both, in a mixture of iodine and acetone on a 1 × 1 cm^2 area was applied. The electric charge on the catalyst in acetone is insufficient for EPD, as very small amounts of free ions exist in acetone. When iodine is used as the dispersant, it can react with acetone through the keto-enol tautomerization to produce protons as per the following equation [Eq. (2)]

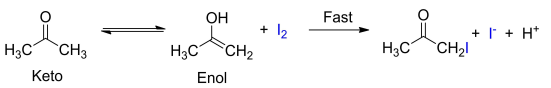

(2)

Thus, formed protons are adsorbed on the surface of the suspended particles by making them positively charged. The applied electric field induces the positively charged particles to migrate towards and deposit on the cathode. Typically, 30 mg of the catalyst powder was suspended in 10 ml acetone and sonicated for 2 h then 2 mg of iodine was added and the suspension sonicated for another 3 min. The EPD was conducted at 10 V for 4 min and thin uniform films were obtained. The sample loading on each NF and FTO was 2 and 1 mg/cm^2, respectively. A similar procedure was also followed to deposit all other electrocatalytically tested compounds.

Faradaic efficiency. The Faradaic efficiency of the materials in 1 M KOH towards oxygen evolution reaction was measured in a two-electrode configuration where nickel foam loaded with the catalysts were used as anode and Pt wire as a cathode in a closed electrochemical cell. The electrolyte and cell were first degassed with Argon for 30 min under stirring. Afterwards, constant current density of 10 mAcm^{-2} or 100 mAcm^{-2} was applied for 8 min or 2 min, respectively. At the end of electrolysis, the gaseous samples were drawn from the headspace by a gas tight syringe and analyzed by a GC calibrated O_2.

The Faradaic efficiency was calculated based on [Eq. (3)]:

$$FE(O_2,\ \%) = \frac{V_{O_2} \times 4 \times F}{V_m \times j \times t} \times 100\,\% \quad (3)$$

V_{o2} is the evolved volume of oxygen, F is the Faraday constant (96485.33289 C/mol), V_m is the molar volume of the gas, j is the current density (10 mAcm^{-2}) and t is the time of electrolysis.

Acknowledgements

We are grateful to the Einstein Center of Catalysis (EC^2) for financial support. This project was also supported by the Deutsche Forschungsgemeinschaft (gefördert im Rahmen der Exzellenzstrategie des Bundes und der Länder – EXC 2008/1 – 390540038 und im Normalverfahren LE 781/19-1).

Conflict of Interest

The authors declare no conflict of interest.

Keywords: oxygen evolution reaction (OER) · stannite · water splitting · iron (Fe) oxyhydroxide · *in situ* transformation

[1] S. Solomon, G.-K. Plattner, R. Knutti, P. Friedlingstein, *Proc. Natl. Acad. Sci. USA* **2009**, *106*, 1704–1709.
[2] Z. W. Seh, J. Kibsgaard, C. F. Dickens, I. Chorkendorff, J. K. Nørskov, T. F. Jaramillo, *Science* **2017**, *355*, 1–12.
[3] S. Chu, Y. Cui, N. Liu, *Nat. Mater.* **2016**, *16*, 16–22.
[4] H. B. Gray, *Nat. Chem.* **2009**, *1*, 7.
[5] F. Lyu, Q. Wang, S. M. Choi, Y. Yin, *Small* **2019**, *15*, 1804201.
[6] N.-T. Suen, S.-F. Hung, Q. Quan, N. Zhang, Y.-J. Xu, H. M. Chen, *Chem. Soc. Rev.* **2017**, *46*, 337–365.
[7] C. Panda, P. W. Menezes, M. Driess, *Angew. Chem. Int. Ed.* **2018**, *57*, 11130–11139; *Angew. Chem.* **2018**, *130*, 11298–11308.
[8] S. Anantharaj, S. R. Ede, K. Sakthikumar, K. Karthick, S. Mishra, S. Kundu, *ACS Catal.* **2016**, *6*, 8069–8097.
[9] P. W. Menezes, C. Panda, C. Walter, M. Schwarze, M. Driess, *Adv. Funct. Mater.* **2019**, *29*, 1808632.
[10] B. R. Wygant, K. Kawashima, C. B. Mullins, *ACS Energy Lett.* **2018**, *3*, 2956–2966.
[11] S. Jin, *ACS Energy Lett.* **2017**, *2*, 1937–1938.

© 2019 The Authors. Published by Wiley-VCH Verlag GmbH & Co. KGaA

[12] C. Walter, P. W. Menezes, S. Orthmann, J. Schuch, P. Connor, B. Kaiser, M. Lerch, M. Driess, *Angew. Chem. Int. Ed.* **2018**, *57*, 698–702; *Angew. Chem.* **2018**, *130*, 706–710.
[13] O. Mabayoje, A. Shoola, B. R. Wygant, C. B. Mullins, *ACS Energy Lett.* **2016**, *1*, 195–201.
[14] C. Panda, P. W. Menezes, M. Zheng, S. Orthmann, M. Driess, *ACS Energy Lett.* **2019**, *4*, 747–754.
[15] A. Dutta, N. Pradhan, *J. Phys. Chem. Lett.* **2017**, *8*, 144–152.
[16] J. S. Kim, B. Kim, H. Kim, K. Kang, *Adv. Energy Mater.* **2018**, *8*, 1–26.
[17] C. Yuan, H. Bin Wu, Y. Xie, X. W. D. Lou, *Angew. Chem. Int. Ed.* **2014**, *53*, 1488–1504; *Angew. Chem.* **2014**, *126*, 1512–1530.
[18] O. Diaz-Morales, I. Ledezma-Yanez, M. T. M. Koper, F. Calle-Vallejo, *ACS Catal.* **2015**, *5*, 5380–5387.
[19] R. Kötz, S. Stucki, *Electrochim. Acta* **1986**, *31*, 1311–1316.
[20] M. Chatti, J. L. Gardiner, M. Fournier, B. Johannessen, T. Williams, T. R. Gengenbach, N. Pai, C. Nguyen, D. R. MacFarlane, R. K. Hocking, A. N. Simonov, *Nat. Can.* **2019**, *2*, 457–465.
[21] I. Katsounaros, S. Cherevko, A. R. Zeradjanin, K. J. J. Mayrhofer, *Angew. Chem. Int. Ed.* **2014**, *53*, 102–121; *Angew. Chem.* **2014**, *126*, 104–124.
[22] M. Hamdani, R. N. Singh, P. Chartier, *Int. J. Electrochem. Sci.* **2010**, *5*, 556–577.
[23] M. S. Burke, L. J. Enman, A. S. Batchellor, S. Zou, S. W. Boettcher, *Chem. Mater.* **2015**, *27*, 7549–7558.
[24] L. Hu, Z. Wu, W. Tian, Y. Jiang, L. Jiang, P. Yang, Z. Pan, *Nanoscale* **2018**, *10*, 12003–12010.
[25] P. Zhang, L. Li, D. Nordlund, H. Chen, L. Fan, B. Zhang, X. Sheng, Q. Daniel, L. Sun, *Nat. Commun.* **2018**, *9*, 1–10.
[26] P. W. Menezes, C. Panda, S. Garai, C. Walter, A. Guiet, M. Driess, *Angew. Chem. Int. Ed.* **2018**, *57*, 15237–15242.
[27] D. A. Corrigan, *J. Electrochem. Soc.* **1987**, *134*, 377.
[28] M. Gong, H. Dai, *Nano Res.* **2015**, *8*, 23–39.
[29] M. S. Burke, S. Zou, L. J. Enman, J. E. Kellon, C. A. Gabor, E. Pledger, S. W. Boettcher, *J. Phys. Chem. Lett.* **2015**, *6*, 3737–3742.
[30] M. Görlin, P. Chernev, J. F. De Araújo, T. Reier, S. Dresp, B. Paul, R. Krähnert, H. Dau, P. Strasser, *J. Am. Chem. Soc.* **2016**, *138*, 5603–5614.
[31] N. Li, D. K. Bediako, R. G. Hadt, D. Hayes, T. J. Kempa, F. von Cube, D. C. Bell, L. X. Chen, D. G. Nocera, *Proc. Mont. Acad. Sci.* **2017**, *114*, 1486–1491.
[32] C. Roy, B. Sebok, S. B. Scott, E. M. Fiordaliso, J. E. Sørensen, A. Bodin, D. B. Trimarco, C. D. Damsgaard, P. C. K. Vesborg, O. Hansen, I. E. L. Stephens, J. Kibsgaard, I. Chorkendorff, *Nat. Can.* **2018**, *1*, 820–829.
[33] B. M. Hunter, N. B. Thompson, A. M. Müller, G. R. Rossman, M. G. Hill, J. R. Winkler, H. B. Gray, *Joule* **2018**, *2*, 747–763.
[34] X.-F. Lu, L.-F. Gu, J.-W. Wang, J.-X. Wu, P.-Q. Liao, G.-R. Li, *Adv. Mater.* **2017**, *29*, 1604437.
[35] R. D. L. Smith, C. Pasquini, S. Loos, P. Chernev, K. Klingan, P. Kubella, M. R. Mohammadi, D. Gonzalez-Flores, H. Dau, *Nat. Commun.* **2017**, *8*, 2022.
[36] B. Zhang, X. Zheng, O. Voznyy, R. Comin, M. Bajdich, M. García-Melchor, L. Han, J. Xu, M. Liu, L. Zheng, *Science* **2016**, *352*, 333–337.
[37] S. Zou, M. S. Burke, M. G. Kast, J. Fan, N. Danilovic, S. W. Boettcher, *Chem. Mater.* **2015**, *27*, 8011–8020.
[38] M. B. Stevens, C. D. M. Trang, L. J. Enman, J. Deng, S. W. Boettcher, *J. Am. Chem. Soc.* **2017**, *139*, 11361–11364.
[39] M. E. G. Lyons, M. P. Brandon, *Int. J. Electrochem. Sci.* **2008**, *3*, 1425–1462.
[40] R. Subbaraman, D. Tripkovic, K. C. Chang, D. Strmcnik, A. P. Paulikas, P. Hirunsit, M. Chan, J. Greeley, V. Stamenkovic, N. M. Markovic, *Nat. Mater.* **2012**, *11*, 550–557.
[41] L. Han, S. Dong, E. Wang, *Adv. Mater.* **2016**, *28*, 9266–9291.
[42] S. Chen, Z. Kang, X. Zhang, J. Xie, H. Wang, W. Shao, X. Zheng, W. Yan, B. Pan, Y. Xie, *ACS Cent. Sci.* **2017**, *3*, 1221–1227.
[43] N. Yang, C. Tang, K. Wang, G. Du, A. M. Asiri, X. Sun, *Nano Res.* **2016**, *9*, 3346–3354.
[44] L. Peng, S. S. A. Shah, Z. Wei, *Chin. J. Catal.* **2018**, *39*, 1575–1593.
[45] M. S. Devi, K. Vidyasagar, *J. Chem. Soc. Dalton Trans.* **2002**, *0*, 2092–2096.
[46] J. W. Lekse, M. A. Moreau, K. L. McNerny, J. Yeon, P. S. Halasyamani, J. A. Aitken, *Inorg. Chem.* **2009**, *48*, 7516–7518.
[47] C. D. Brunetta, J. A. Brant, K. A. Rosmus, K. M. Henline, E. Karey, J. H. MacNeil, J. A. Aitken, *J. Alloys Compd.* **2013**, *574*, 495–503.
[48] H. Hahn, H. Schulze, *Naturwissenschaften* **1965**, *52*, 426.
[49] R. Nitsche, D. F. Sargent, P. Wild, *J. Cryst. Growth* **1967**, *1*, 52–53.
[50] W. Schäfer, R. Nitsche, *Mater. Res. Bull.* **1974**, *9*, 645–654.
[51] R. Caye, Y. Laurent, P. Picot, R. Pierrot, C. Lévy, *Bull. Soc. Fr. Mineral. Cristallogr.* **1968**, *91*, 383–387.
[52] A. M. Lamarche, A. Willsher, L. Chen, G. Lamarche, J. C. Woolley, *J. Solid State Chem.* **1991**, *94*, 313–318.
[53] K. Ito, T. Nakazawa, *Jpn. J. Appl. Phys.* **1988**, *27*, 2094–2097.
[54] A. M. Alanazi, F. Alam, A. Salhi, M. Missous, A. G. Thomas, P. O'Brien, D. J. Lewis, *RSC Adv.* **2019**, *9*, 24146–24153.
[55] Y. Xie, C. Zhang, G. Yang, J. Yang, X. Zhou, J. Ma, *J. Alloys Compd.* **2017**, *696*, 938–946.
[56] T. Shibuya, Y. Goto, Y. Kamihara, M. Matoba, K. Yasuoka, L. A. Burton, A. Walsh, *Appl. Phys. Lett.* **2014**, *104*, 021912.
[57] N. Nakayama, K. Ito, *Appl. Surf. Sci.* **1996**, *92*, 171–175.
[58] M. Ganchev, J. Iljina, L. Kaupmees, T. Raadik, O. Volobujeva, A. Mere, M. Altosaar, J. Raudoja, E. Mellikov, *Thin Solid Films* **2011**, *519*, 7394–7398.
[59] Y. B. Kishore Kumar, G. Suresh Babu, P. Uday Bhaskar, V. Sundara Raja, *Sol. Energy Mater. Sol. Cells* **2009**, *93*, 1230–1237.
[60] A. Ritscher, J. Just, O. Dolotko, S. Schorr, M. Lerch, *J. Alloys Compd.* **2016**, *670*, 289–296.
[61] N. K. Chaudhari, H. Jin, B. Kim, K. Lee, *Nanoscale* **2017**, *9*, 12231–12247.
[62] P. W. Menezes, C. Panda, S. Loos, F. Bunschei-Bruns, C. Walter, M. Schwarze, X. Deng, H. Dau, M. Driess, *Energy Environ. Sci.* **2018**, *11*, 1287–1298.
[63] T. Shinagawa, A. T. Garcia-Esparza, K. Takanabe, *Sci. Rep.* **2015**, *5*, 1–21.
[64] C. Costentin, D. K. Bediako, D. G. Nocera, J.-M. Savéant, E. C. Jones, *J. Am. Chem. Soc.* **2013**, *135*, 10492–10502.
[65] C. P. Andrieux, J. M. Dumas-Bouchiat, J. M. Savéant, *J. Electroanal. Chem. Interfacial Electrochem.* **1982**, *131*, 1–35.
[66] R. L. Doyle, M. E. G. Lyons, *Phys. Chem. Chem. Phys.* **2013**, *15*, 5224.
[67] D. E. Janney, J. M. Cowley, P. R. Buseck, *Clays Clay Miner.* **2000**, *48*, 111–119.
[68] R. K. Kukkadapu, J. M. Zachara, J. K. Fredrickson, S. C. Smith, A. C. Dohnalkova, C. K. Russell, *Am. Mineral.* **2003**, *88*, 1903–1914.
[69] S. K. Chawla, N. Sankarraman, J. H. Payer, *J. Electron Spectrosc. Relat. Phenom.* **1992**, *61*, 1–18.
[70] N. S. McIntyre, D. G. Zetaruk, *Anal. Chem.* **1977**, *49*, 1521–1529.
[71] H. Abdel-Samad, P. R. Watson, *Appl. Surf. Sci.* **1997**, *108*, 371–377.
[72] J. Liu, M. Zheng, X. Shi, H. Zeng, H. Xia, *Adv. Funct. Mater.* **2016**, *26*, 919–930.
[73] L. Shen, Y. Cao, Z. Du, W. Zhao, K. Lin, L. Jiang, *Appl. Surf. Sci.* **2017**, *425*, 212–219.
[74] F. Gilbert, P. Refait, F. Lévêque, C. Remazeilles, E. Conforto, *J. Phys. Chem. Solids* **2008**, *69*, 2124–2130.
[75] P. W. Menezes, A. Indra, I. Zaharieva, C. Walter, S. Loos, S. Hoffmann, R. Schlögl, H. Dau, M. Driess, *Energy Environ. Sci.* **2019**, *12*, 988–999.
[76] L. Debeer-Schmitt, K. C. Littrell, M. A. McGuire, W. M. Chance, L. Li, J. Ermentrout, A. S. Sefat, *Phys. C* **2017**, *534*, 29–36.
[77] H. M. Rietveld, *J. Appl. Crystallogr.* **1969**, *2*, 65–71.
[78] J. Rodriguez-Carvajal, FULLPROF: a Progr. Rietveld Refinement Pattern Matching analysis, collected abstracts of the meeting powder diffraction, Toulouse, **1990**, p. 127..
[79] C. C. L. McCrory, S. Jung, J. C. Peters, T. F. Jaramillo, *J. Am. Chem. Soc.* **2013**, *135*, 16977–16987.
[80] C. C. L. McCrory, S. Jung, I. M. Ferrer, S. M. Chatman, J. C. Peters, T. F. Jaramillo, *J. Am. Chem. Soc.* **2015**, *137*, 4347–4357.
[81] S. Anantharaj, S. R. Ede, K. Karthick, S. Sam Sankar, K. Sangeetha, P. E. Karthik, S. Kundu, *Energy Environ. Sci.* **2018**, *11*, 744–771.
[82] R. Beltrán-Suito, P. W. Menezes, M. Driess, *J. Mater. Chem. A* **2019**, *7*, 15749–15756.
[83] N. Koura, T. Tsukamoto, HiromasaShoji, T. Hotta, *Jpn. J. Appl. Phys.* **1995**, *34*, 1643–1647.
[84] C. Panda, P. W. Menezes, S. Yao, J. Schmidt, C. Walter, J. N. Hausmann, M. Driess, *J. Am. Chem. Soc.* **2019**, *141*, 13306–13310.

Manuscript received: September 9, 2019
Revised manuscript received: November 15, 2019
Accepted manuscript online: November 17, 2019
Version of record online: January 9, 2020

© 2019 The Authors. Published by Wiley-VCH Verlag GmbH & Co. KGaA